Available online at www.sciencedirect.com

ScienceDirect

Energy Procedia 160 (2019) 428–435

Energy Procedia

www.elsevier.com/locate/procedia

2nd International Conference on Energy and Power, ICEP2018, 13–15 December 2018, Sydney, Australia

Numerical study on inertial effects on liquid-vapor flow using lattice Boltzmann method

Shurong Lei[a], Yong Shi[a,*], Yuying Yan[b], Xingxing Zhang[c]

[a]*Department of Mechanical, Materials and Manufacturing Engineering, University of Nottingham Ningbo China, Ningbo 315100, China*
[b]*Research Group of Fluids and Thermal Engineering, Faculty of Engineering,University of Nottingham, Nottingham NG7 2RD, United Kingdom*
[c]*School of Industrial Technologies and Business Studies, Dalarna University, Falun 79188, Sweden*

Abstract

Liquid-vapor flow in porous media is studied in this article. To fulfill this goal, a double-distribution-function lattice Boltzmann (LB) model is proposed based on the separate-phase governing equations at the representative elementary volume (REV) scale. Importantly, besides the Darcy force and capillary force, which were commonly included in previous studies, the LB model in this article also considers the inertial force characterized by the Forchheimer term. This feature enables the model to offer an effective description of liquid-vapor flow in porous media at low, intermediate and even high flow rates. We validated the LB model by simulating a single-phase flow in porous media driven by a pressure difference and found its results are in good agreement with the available analytical solutions. We then applied the model to study water-vapor flow in a semi-infinite porous region bounded by an impermeable and heated wall. The numerical simulation reveals the flow and mass transfer characteristics under the compounding effects of inertial, Darcy and capillary forces. Through a comparison with the results given by the generalized Darcy's law, our numerical results directly evidence that the inertial force is a dominating factor when a fluid passes through porous media at an intermediate or high flow rate.

Keywords: Lattice Botlzmann method; inertial effects; liquid-vapor flow; porous media

* Corresponding author. Tel.: +86-(0)574-88180000-9413; fax: +86-(0)574-88180715.
E-mail address: Yong.Shi@nottingham.edu.cn

10.1016/j.egypro.2019.02.177

Nomenclature

Symbols

Ca	Capillary number ($= \mu_0 u_0 / \sigma$)
Da	Darcy number ($= K / L_0^2$)
K	permeability (m^2)
k_r	relative permeability
Ma	Mach number ($= u_0 / c_s$)
p	pressure (Pa)
Re	Reynolds number ($= \rho_l u_0 L_0 / \mu_l$)
s	saturation
$\mathbf{u}$	superficial velocity ($\mathrm{m/s}$)
u	velocity component in the x direction ($\mathrm{m/s}$)
v	velocity component in the y direction ($\mathrm{m/s}$)
ε	porosity
ρ	density ($\mathrm{kg/m^3}$)
ρ^*	density ratio ($= \rho_v / \rho_l$)
β	inertial resistance factor ($= 1/\mathrm{m}$)
μ	dynamics viscosity ($\mathrm{Pa \cdot s}$)
σ	interfacial tension ($\mathrm{N/m}$)
μ^*	viscosity ratio ($= \mu_v / \mu_l$)

Subscripts

l	liquid
v	vapor
m	mixture
c	capillary
0	reference state

Uppercases

P	dimensionless pressure ($= p / p_0$)
$\mathbf{U}$	dimensionless velocity ($= \mathbf{u} / u_0$)
$\mathbf{X}$	dimensionless coordinate ($= \mathbf{x} / L_0$)

1. Introduction

Porous media containing liquid and vapor ubiquitously exist in a large variety of natural resources and modern applications in energy engineering [1,2]. An elaboration of these complex multiphase flows at the pore scale calls for accurate resolutions of the underlying porous solid skeletons, which are practically unavailable in many scenarios. Alternatively, a simple mathematical description averaged over the so-called representative elementary volume (REV) was developed to capture effective gross flow characteristics without the underlying pore-scale details [3]. One of the most representative REV-scale models is Darcy equation [4]. However, this equation is found insufficiently accurate in intermediate and high flow-rate problems, e.g., oil and gas recovery in open fractures [5] where the inertial force plays an important role. Therefore, this work will focus on liquid-vapor flow in porous media with co-existence of the Darcy, inertial and capillary forces. We aim at developing a robust and efficient lattice Boltzmann (LB) model to investigate the interplay among these forces and revealing the inertial effects at the REV scale on two-phase flow and mass transfer in porous media where the flow rate is large.

The LB method has attracted tremendous interests over the past several decades owing to its unique and super merits in modeling fluid transport phenomena [6,7]. These include its simple coding, flexible boundary treatments for complex boundaries and intrinsic parallel-computing algorithmic structure, to name a few. Importantly, the method has been widely applied to simulate flow in porous media at both the REV and pore scales [8,9,10]. At the pore scale, the LB studies on liquid-vapor flow are usually interested in constructing a model with an explicit presence of liquid, vapor and solid interfaces [9]. These studies focus on capturing bubbles' or droplets' movement and deformation in the pore networks. As to the LB models at the REV scale, to achieve simple mathematics and reasonable numerical efficiency, these models smear out the pore-scale details and only describe the effective averaged transport characteristics [8]. In particular, the REV scale LB models for liquid-vapor two phase flow can be further classified into the "mixture models" [11] and "separate-phase models". The former treats the liquid and vapor as a homogeneous mixture with a set of effective mixture properties, whereas the latter describes each phase using different governing equations with its own properties. It should be pointed out that the inertial force in terms of the Forchheimer term is hard to cast into the mixture framework. Due to this reason, this article will construct a LB model for liquid vapor two-phase flow in porous media considering the inertial effects based on the separate-phase governing equations. To be specific, we will propose a double-distribution-function LB model to describe liquid and vapor flow in porous media

at the REV scale, respectively. We will then validate the model by simulating single-phase flow through porous media driven by a pressure difference and apply it to simulate water-vapor flow in a semi-infinite porous region afterwards. The numerical results in this work will reveal liquid-vapor flow and mass transfer characteristics in porous media with the inertial effects, which were usually ignored in the previous studies.

This article is organized as follows: we first introduce the REV-scale separate-phase governing equations for liquid-vapor flow in porous media in Section 2. In Section 3, the corresponding LB model is proposed. Such a model is validated in Section 4 and then extended to study water-vapor flow in porous media with phase change at the wall. Finally, we draw the conclusion in Section 5.

2. Separate-phase governing equations at the REV scale for liquid-vapor flow in porous media

Consider a liquid and its vapor flow through isotropic and homogeneous porous media. At the REV scale, mass transfer and flow of each phase are described by the following governing equations [12],

$$\frac{\partial}{\partial \mathbf{x}} \cdot \mathbf{u}_l = 0 \tag{1}$$

$$\frac{\mu_l \mathbf{u}_l}{K k_{rl}} + \rho_l \beta_l \left|\mathbf{u}_l\right| \mathbf{u}_l = -\frac{\partial p_l}{\partial \mathbf{x}} \tag{2}$$

$$\frac{\partial}{\partial \mathbf{x}} \cdot \mathbf{u}_v = 0 \tag{3}$$

$$\frac{\mu_v \mathbf{u}_v}{K k_{rv}} + \rho_v \beta_v \left|\mathbf{u}_v\right| \mathbf{u}_v = -\frac{\partial p_v}{\partial \mathbf{x}} \tag{4}$$

where the liquid and vapor relative permeabilities $k_{rl} = s^3$ and $k_{rv} = (1-s)^3$ [4], and their inertial resistance factors $\beta_l = 0.005/\sqrt{Kk_{rl}}/(\varepsilon s)^{5.5}$ and $\beta_v = 0.005/\sqrt{Kk_{rv}}/(\varepsilon - \varepsilon s)^{5.5}$ [12]. In this article, the velocities of the liquid and vapor phases, $\mathbf{u}_l$ and $\mathbf{u}_v$, are the superficial averages while their pressures are defined as the intrinsic averages. Moreover, p_v and p_l are linked by the capillary pressure, which is computed by $p_c = p_v - p_l = \sqrt{\varepsilon/K}\sigma\left(-1.263s^3 + 1.669s^2 - 0.966s + 0.56\right)$ [4]. Note that the reason why we define the relative permeability and inertial resistance factor as above is for a direct comparison of our results to those in previous work [4]. Other expressions for these parameters are applicable provided that they give a more precise prediction.

Significantly, to better analyze the involved multiphase flow and mass transfer, Eqs. (1)–(4) should be rewritten in a dimensionless form. By introducing the characteristic length L_0, characteristic velocity u_0, characteristic pressure $p_0 = \mu_l u_0 L_0 / K$, we have

$$\frac{\partial}{\partial \mathbf{X}} \cdot \mathbf{U}_l = 0 \tag{5}$$

$$\mathbf{U}_l + \frac{\alpha}{\varepsilon^{5.5} s^4} \mathrm{Re}\sqrt{Da}\left|\mathbf{U}_l\right| \mathbf{U}_l = -s^3 \frac{\partial P_l}{\partial X} \tag{6}$$

$$\frac{\partial}{\partial \mathbf{X}} \cdot \mathbf{U}_v = 0 \tag{7}$$

$$\mathbf{U}_v + \frac{\rho^*}{\mu^*} \frac{\alpha}{\varepsilon^{5.5}(1-s)^4} \mathrm{Re}\sqrt{Da}\left|\mathbf{U}_v\right| \mathbf{U}_v = -\frac{(1-s)^3}{\mu^*} \frac{\partial P_v}{\partial \mathbf{X}} \tag{8}$$

Here $\alpha = 0.005$. Interestingly, Eqs. (5)–(8) can be further reduced—We take the divergence to Eqs. (6) and (8), and substitute Eqs. (5) and (7) into the resulting equations. After several manipulations, a set of the reduced governing equations in terms of P_l and s are obtained

$$\frac{\partial_1}{\partial \mathbf{X}}\cdot\left(s^3\frac{\partial P_l}{\partial \mathbf{X}}\right) = -\frac{\alpha\,\mathrm{Re}\sqrt{Da}}{\varepsilon^{5.5}}\frac{\partial_1}{\partial \mathbf{X}}\cdot\left(\frac{|\mathbf{U}_l|\mathbf{U}_l}{s^4}\right) \tag{9}$$

$$\frac{\partial_1}{\partial \mathbf{X}}\cdot\left[(1-s)^3\frac{\partial P_l}{\partial \mathbf{X}}\right] = -\frac{\alpha\rho^*\,\mathrm{Re}\sqrt{Da}}{\varepsilon^{5.5}}\frac{\partial_1}{\partial \mathbf{X}}\cdot\left[\frac{|\mathbf{U}_v|\mathbf{U}_v}{(1-s)^4}\right] + \frac{\sqrt{\varepsilon Da}}{Ca}\frac{\partial_1}{\partial \mathbf{X}}\cdot\left[P_5(s)\frac{\partial s}{\partial \mathbf{X}}\right] \tag{10}$$

where the fifth-order polynomial $P_5(s) = -3.789s^5 + 14.705s^4 - 22.347s^3 + 16.701s^2 - 6.236s + 0.966$. Note that in the next section, we will numerically solve Eqs. (9) and (10), rather than Eqs. (5)–(8), using the LB method. Once P_l and s are obtained, the velocities $\mathbf{U}_l$ and $\mathbf{U}_v$ are then specified by Eqs. (6) and (7). The latter just involves algebraic operations and can be solved directly.

3. Lattice Boltzmann model

To solve Eqs. (9) and (10), a double-distribution-function LB model is proposed in this section. For simplicity while without loss of generality, we only consider two-dimensional (2D) problems. The evolution equations of the LB model are

$$f_i(\mathbf{x}+\mathbf{c}_i\Delta t, t+\Delta t) - f_i(\mathbf{x},t) = -1/\tau_f\left[f_i(\mathbf{x},t) - f_i^{eq}(\mathbf{x},t)\right] + \Delta t F_i \tag{11}$$

$$g_i(\mathbf{x}+\mathbf{c}_i\Delta t, t+\Delta t) - g_i(\mathbf{x},t) = -1/\tau_g\left[g_i(\mathbf{x},t) - g_i^{eq}(\mathbf{x},t)\right] + \Delta t G_i \tag{12}$$

where f_i and g_i are the two distribution functions in terms of the discrete velocity $\mathbf{c}_i$. τ_f and τ_g are the corresponding dimensionless relaxation times. The equilibrium distributions and external-force terms in the right side of Eqs. (11) and (12) are

$$f_i^{eq} = \omega_i P_l \qquad g_i^{eq} = \omega_i s \tag{13}$$

$$F_i = -\frac{\omega_i}{\tau_f c_s^2 \Delta t}\frac{\alpha\,\mathrm{Re}\sqrt{Da}}{\varepsilon^{5.5}s^4}|\mathbf{U}_l|\mathbf{U}_l\cdot\mathbf{c}_i \qquad G_i = \frac{\omega_i}{\tau_g c_s^2 \Delta t}\left[\frac{\alpha\rho^*\,\mathrm{Re}\sqrt{Da}}{\varepsilon^{5.5}(1-s)^4}|\mathbf{U}_v|\mathbf{U}_v + (1-s)^3\frac{\partial P_l}{\partial \mathbf{X}}\right]\cdot\mathbf{c}_i \tag{14}$$

In Eqs. (13)–(14), ω_i is the moment weight corresponding to $\mathbf{c}_i$. They are specified by the D2Q9 scheme [13]. In our LB model, the saturation and liquid pressure are computed using $s = \sum_{i=0}^{8} g_i$ and $P_l = \sum_{i=0}^{8} f_i$. In numerical implementation, the above LB model will compute s^n and P_l^n at the n^{th} step with $\mathbf{U}_l^{n-1}$ and $\mathbf{U}_v^{n-1}$ from the last time step. $\mathbf{U}_l^n$ and $\mathbf{U}_v^n$ will then update through solving Eqs. (6) and (8) directly. The whole simulation won't terminate until the convergence is reached.

4. Results and discussions

4.1. Single-phase flow in porous media

We first validate the LB model in Section 3 by simulating a single-phase flow in porous media, see Fig. 1. The reason we chose this case is because its analytical solutions are available. In this problem, a fluid flows through porous

media confined in a domain with a characteristic length L_0. The inlet and outlet pressures are P_{in} and P_{out} while periodic boundary conditions are imposed at the domain's top and bottom boundaries. The streamwise superficial velocity (component in the x direction) is then solved [14].

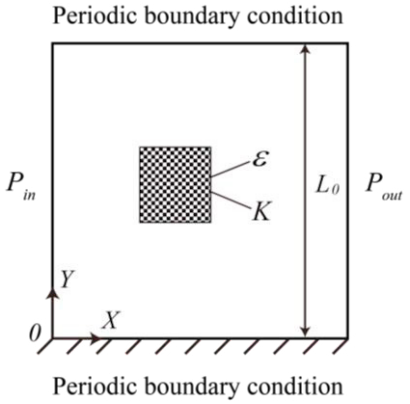

Fig. 1. Schematic of the single-phase flow in porous media. The origin of the coordinates is at the left bottom corner.

$$U=\frac{-1+\sqrt{1-0.02\,\mathrm{Re}\sqrt{Da}/\varepsilon^{5.5}\cdot dP/dX}}{0.01\,\mathrm{Re}\sqrt{Da}/\varepsilon^{5.5}} \qquad V=0 \tag{15}$$

where U and V are the velocity components in the X and Y directions.

We carried out the LB simulations on 100×100 grids subject to the boundary conditions $P_{in}=1$ and $P_{out}=0$. These pressure boundary conditions were implemented in our algorithm by the non-equilibrium extrapolation method [15]. Meanwhile, the periodic boundary treatments were employed on the top and bottom boundaries. As to the relaxation time, we specified it as $\tau_f=s^3\Big/\left(c_s^2\Delta t\right)+0.5=0.6732$, resulting in $Ma=0.001$. In addition, we set $Da=0.001$, $\varepsilon=0.5$ and $\mathrm{Re}=0.001$, 10, 30 and 50. In simulation, all the results were justified by the grid-independence tests.

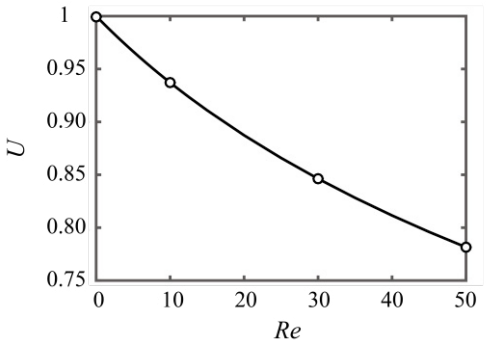

Fig. 2. The streamwise velocities with different Reynold numbers. Solid line: analytical solutions; open circles: LB results.

Figure 2 shows the streamwise velocities obtained by our LB simulations with different Reynolds numbers, together with the corresponding analytical solutions. It is seen that the numerical results are well agreed with those analytical solutions. Note that in the limit of $\mathrm{Re}=0$, at which the flow rate is very small, Darcy's law should be held. Figure 2 exhibits the obtained dimensionless streamwise velocity under that condition $U=1$. This is the very solution to the Darcy equation. Meanwhile, when Re increases, U in Fig. 2 gets smaller and smaller. This indicates at intermediate and high flow rates, the inertial effects represented by the Forchheimer term are not trivial.

4.2. Water-vapor two-phase flow in a semi-infinite porous region

Next, we apply the LB model to simulate water-vapor flow in a semi-infinite region occupied by isotropic and homogeneous porous media with porosity ε and permeability K, see Fig. 3. To be specific, consider liquid water flows into the porous media, and at the bottom there is a plain heated plate. Phase change occurs on this plate where liquid water turns into vapor. In order to compare with the results in Ref. [4], we assume a uniform saturation $s=0.8$ on the bottom plate, and set other boundary conditions as $X=0:\ U_l=1,\ s=1;\ X=1:\ \partial U_l/\partial X=0,\ \partial s/\partial X=0;$ $Y=0:\ V_l=-\rho^* V_v,\ s=0.8$ and $Y=1:\ U_l=1,\ s=1$.

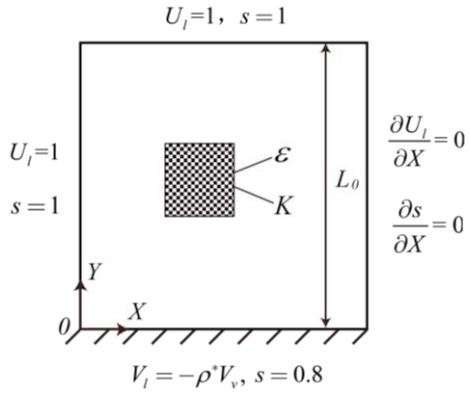

Fig. 3. Schematic of the water-vapor flow in a semi-infinite porous region. The origin of the coordinates is at the left bottom corner.

Again, we conducted the LB simulation on 100×100 grids and specified the density and viscosity ratios $\rho^*=6.23\times10^{-4}$ and $\mu^*=4.25\times10^{-2}$, referring to water and its vapor's states at the standard atmospheric pressure [4]. In simulation, $Ma=0.001$, $Da=0.001$, $\varepsilon=0.5$ and $Ca=0.1$. The Reynolds number ranges from 0.001 to 50. Moreover, to compare with the results in Ref. [4], we introduced the mixture momentum $\rho_m\mathbf{U}_m=\mathbf{U}_l+\rho^*\mathbf{U}_v$ with the mixture density $\rho_m=1+(1-s)\rho^*$, and computed its values based on our LB results. We also introduced the transform coordinate $\eta=\sqrt{Ca}Y\big/\sqrt[4]{\varepsilon DaX^2}$ and a scaling factor $\xi=\sqrt[4]{Ca^2X^2\big/\varepsilon Da}$ for the velocity component in the Y direction in our following discussion [4].

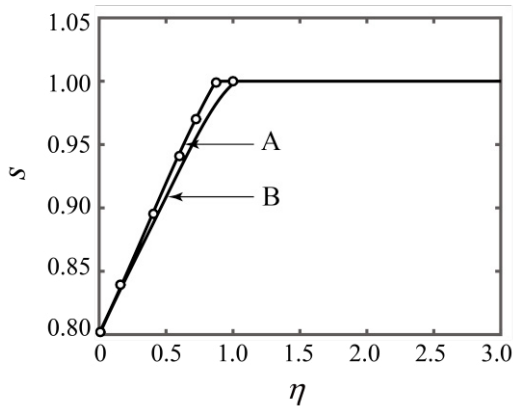

Fig. 4. The saturation distributions with different Reynold numbers. Line A: LB results at $\mathrm{Re}=0.001$; line B: LB results at $\mathrm{Re}=50$; open circles: results from Ref. [4].

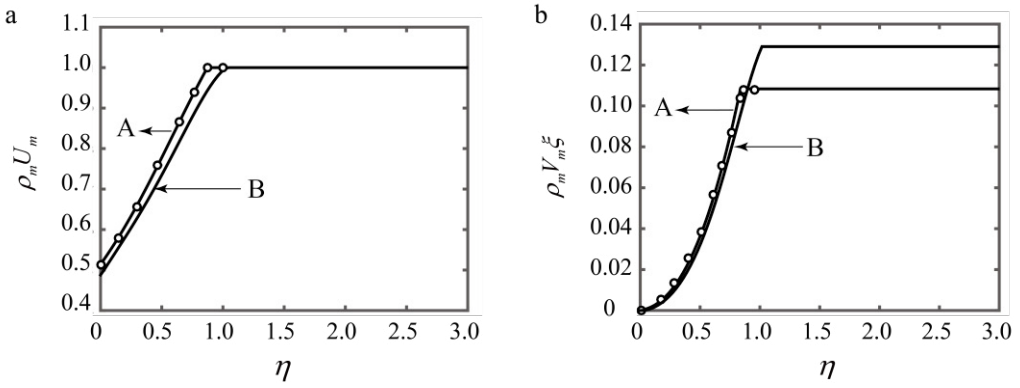

Fig. 5. (a) the streamwise mixture momentum; (b) the cross-streamwise mixture momentum. Line A: LB results at $\mathrm{Re} = 0.001$; line B: LB results at $\mathrm{Re} = 50$; open circles: results from Ref. [4].

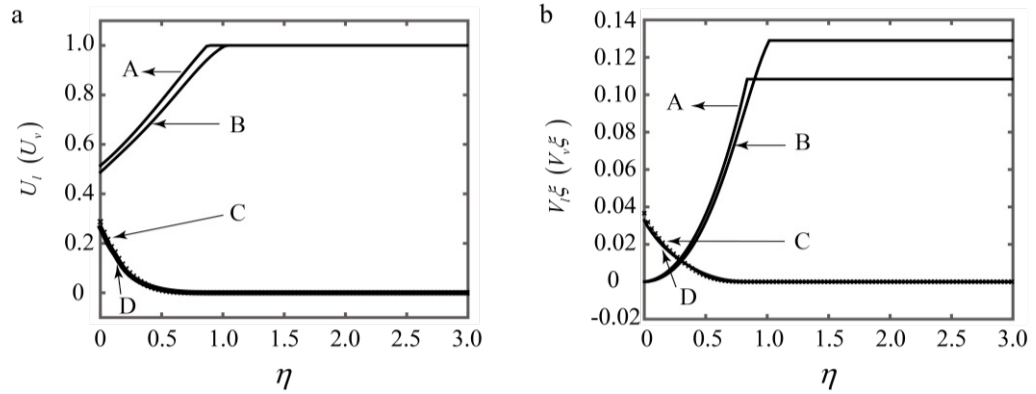

Fig. 6. (a) the streamwise velocity; (b) the cross-streamwise velocity. Line A: liquid velocity at $\mathrm{Re} = 0.001$; line B: Liquid velocity at $\mathrm{Re} = 50$; cross C: vapor velocity at $\mathrm{Re} = 0.001$; line D: vapor velocity at $\mathrm{Re} = 50$.

Figure 4 exhibits the saturation distributions obtained from the LB simulations at different Reynolds numbers. For demonstration, the figure only displays the results when $\mathrm{Re} = 0.001$ and $\mathrm{Re} = 50$, together with those from Ref. [4] using the generalized Darcy's law without the Forchheimer term. It is found that saturation grows from its boundary value $s = 0.8$ to its bulk value $s = 1$ in all cases. In particular, saturation is smaller than one but larger than its boundary value in the vicinity of the plate, indicating there is a two-phase flow zone involving both liquid water and its vapor. Interestingly, we see the saturation profiles depend on the Reynolds number. When Re is small, say $\mathrm{Re} = 0.001$, the LB results are in good agreement with those from Ref. [4]. However, when Re grows, a deviation in s from the Darcy profile is observed in the two-phase zone. This demonstrates that the inertial effects on liquid-vapor mass transfer are nontrivial when the Reynolds number is finite. In this scenario, the generalized Darcy's law is not sufficiently accurate any more.

Figures 5 and 6 further show the mixture momentum, liquid and vapor velocities along the η direction. In Figs. 5(a) and 6(a), we see the streamwise mixture momentum and liquid velocity decay when moving from the bulk region to the plate. Meanwhile, both of them have an apparent slip on the wall. The decay phenomenon occurs in the two-phase zone and results from the decrease of saturation. For the streamwise vapor velocity, it is shown its maximum appears at the wall where phase change occurs and then gradually decreases to zero in the bulk flow region. Figures 5(b) and 6(b) also show the cross-streamwise mixture momentum, liquid and vapor velocities. A careful observation can identify the zero cross-streamwise mixture momentum at the wall as the wall is impermeable. However, both the liquid and vapor cross-streamwise velocities at the wall are nonzero. This is not surprising since phase change takes place at the wall, at which water turns into vapor.

It should also be noted that both figures compare the flow characteristics when $\mathrm{Re}=0.001$ and $\mathrm{Re}=50$. Due to the existence of inertial force, the mixture momentum and liquid velocity display clear differences when the Reynolds number grows. Interestingly, the vapor flows shown in Figs. 6(a) and 6(b) are nearly insensitive with the changing Re—The results of $\mathrm{Re}=50$ almost overlap those of $\mathrm{Re}=0.001$. We analyze this is because the Reynolds number used in this work is defined as $\mathrm{Re}=\rho_l u_0 L_0/\mu_l$ depending on the liquid properties. For the vapor phase, its own Reynolds number should be $\rho^*/\mu^*\,\mathrm{Re}$. In our studies, $\rho^*/\mu^*\,\mathrm{Re}$ is very small regardless of $\mathrm{Re}=0.001$ or $\mathrm{Re}=50$. It is expected that the inertial effects in the vapor phase would become significant when $\rho^*/\mu^*\,\mathrm{Re}$ is large enough.

4. Conclusion

In this article, we developed a double-distribution-function LB model to study numerically liquid vapor two-phase transport characteristics at the REV scale. Different from those previous studies, our model considers the compounding effects resulted from the Darcy, capillary and inertial forces. The numerical results indicate that the inertial force will be significant when the flow rate is intermediate or high. Importantly, the simulations in this article demonstrate the proposed LB model is a useful tool to capture both single-phase and two-phase flow and mass transfer with the inertial effects in porous media.

Acknowledgements

This research was supported by Zhejiang Provincial Natural Science Foundation of China under Grant No. LY16E060001, Ningbo Science and Technology Bureau Technology Innovation Team (Grant No. 2016B10010) and Ningbo International Cooperation Program (Grant No. 2015D10018).

References

[1] Sakai, Masaru, Nobuo Toride, and Jiří Šimůnek. "Water and vapor movement with condensation and evaporation in a sandy column." *Soil Science Society of America Journal* 73(3) (2009): 707-717.

[2] Mori, Shoji, and Kunito Okuyama. "Enhancement of the critical heat flux in saturated pool boiling using honeycomb porous media." *International Journal of Multiphase Flow* 35(10) (2009): 946-951.

[3] Whitaker, Stephen. "Flow in porous media II: The governing equations for immiscible, two-phase flow." *Transport in porous media* 1(2) (1986): 105-125.

[4] Chao-Yang, Wang, and C. Beckermann. "A two-phase mixture model of liquid-gas flow and heat transfer in capillary porous media—II. Application to pressure-driven boiling flow adjacent to a vertical heated plate." *International journal of heat and mass transfer* 36(11) (1993): 2759-2768.

[5] Fourar, M., and R. Lenormand. "A new model for two-phase flows at high velocities through porous media and fractures." *Journal of Petroleum Science and Engineering* 30(2) (2001): 121-127.

[6] Shi, Yong, and John E. Sader. "Lattice Boltzmann method for oscillatory Stokes flow with applications to micro-and nanodevices." *Physical Review E* 81(3) (2010): 036706..

[7] Kang, Hang, Yong Shi, and Yuying Yan. "Block iterative frequency-based lattice Boltzmann algorithm for microscale oscillatory flow." *Computers & Fluids* 167 (2018): 196-205.

[8] Guo, Zhaoli, and T. S. Zhao. "Lattice Boltzmann model for incompressible flows through porous media." *Physical Review E* 66(3) (2002): 036304.

[9] Hao, Liang, and Ping Cheng. "Pore-scale simulations on relative permeabilities of porous media by lattice Boltzmann method." *International Journal of Heat and Mass Transfer* 53(9-10) (2010): 1908-1913.

[10] Liu, Minghua, et al. "Lattice Boltzmann simulation of flow and heat transfer in random porous media constructed by simulated annealing algorithm." *Applied Thermal Engineering* 115 (2017): 1348-1356.

[11] Lei, Shurong, Yong Shi, and Yuying Yan. "Lattice Boltzmann mixture model for liquid-vapor flow with phase change in porous media." *Proceedings of the 16th International Heat Transfer Conference (IHTC16) 2018*; Beijing, China.

[12] Ahmadi, Azita, Ali Akbar Abbasian Arani, and Didier Lasseux. "Numerical simulation of two-phase inertial flow in heterogeneous porous media." *Transport in porous media* 84(1) (2010): 177-200.

[13] Qian, Y. H., Dominique d'Humières, and Pierre Lallemand. "Lattice BGK models for Navier-Stokes equation." *Europhysics Letters* 17(6) (1992): 479-484.

[14] Awartani, M. M., and M. H. Hamdan. "Fully developed flow through a porous channel bounded by flat plates." *Applied mathematics and computation* 169(2) (2005): 749-757.

[15] Guo, Zhao-Li, Chu-Guang Zheng, and Bao-Chang Shi. "Non-equilibrium extrapolation method for velocity and pressure boundary conditions in the lattice Boltzmann method." *Chinese Physics* 11(4) (2002): 366-374.